Arabian Journal of Chemistry (2022) **15**, 104326

King Saud University

Arabian Journal of Chemistry

www.ksu.edu.sa
www.sciencedirect.com

ORIGINAL ARTICLE

Irreversibility analysis of Ellis hybrid nanofluid with surface catalyzed reaction and multiple slip effects on a horizontal porous stretching cylinder

Muhammad Naveed Khan [a,*], Nevzat Akkurt [b], N. Ameer Ahammad [c], Shafiq Ahmad [a], Abdelfattah Amari [d,e], Sayed M Eldin [f], Amjad Ali Pasha [g]

[a] *Department of Mathematics, Quaid-I-Azam University, Islamabad Pakistan*
[b] *Munzur University Department of Mechanical Engineering 62000, Tunceli Turkey*
[c] *Department of Mathematics, Faculty of Science, University of Tabuk, P.O. Box. 741, Tabuk 71491, Saudi Arabia*
[d] *Department of Chemical Engineering, College of Engineering, King Khalid University, Abha 61411, Saudi Arabia*
[e] *Research Laboratory of Processes, Energetics, Environment and Electrical Systems, National School of Engineers of Gabes, Gabes University, Gabes 6072, Tunisia*
[f] *Center of Research, Faculty of Engineering, Future University in Egypt, New Cairo 11835, Egypt*
[g] *Aerospace Engineering Department, King Abdulaziz University, Jeddah 21589, Saudi Arabia*

Received 27 June 2022; accepted 2 October 2022
Available online 7 October 2022

KEYWORDS

Ellis's hybrid nanofluid;
Slip boundary conditions;
Heat generation/absorption;
Nonlinear thermal radiation;
Surface catalyzed reaction;
Homogeneous and heterogeneous reactions

Abstract This paper presents the theoretical and computation irreversibility investigation of the Ellis hybrid nanofluid flow ($CuO - Al_2O_3$ nanoparticles) model using both homogeneous and heterogeneous responses toward the horizontal porous stretching cylinder. The Joule heating, thermal radiation, and heat generation/absorption are all factors that affect thermal energy transport, all of which are explored. On the surface of the cylinder, the slip boundary conditions are enforced. Keeping in mind that the nonlinear partial differential equations (PDEs) are converted into nonlinear ordinary differential equations (ODEs), these ODEs are constructed from the mathematical flow model with the aid of proper transformations. With the help of the bvp4c MATLAB built-in method, the nonlinear system equations are tacked numerically. Graphical results are used to discuss the numerical aspects of different parameters. By increasing the curvature parameter, entropy generation increases while fluid velocity decreases. Elasticity and magnetic fields thin boundary layers. Realistically, as liquid porosity increases, momentum boundary layer diminishes.

* Corresponding author.
E-mail address: mnkhan@math.qau.edu.pk (M. Naveed Khan).
Peer review under responsibility of King Saud University.

Production and hosting by Elsevier

https://doi.org/10.1016/j.arabjc.2022.104326

Nomenclature

u, w	velocity components [ms^{-1}]	(τ_0, α_1)	material constant
T	fluid temperature [K]	S_c	Schmidt number
T_∞	ambient temperature [K]	E_c	Eckert number
M	magnetic parameter	β	material parameter
Pr	Prandtl number	γ	curvature parameter
E_c	Eckert number	S_b	bioconvection Schmidt number
R_d	thermal radiation	P_e	Peclet number
(D_A^*, D_B^*)	diffusion coefficient	k_{hnf}	thermal conductivity [kgmK^{-1} s^{-3}]
S_1	suction parameter	v_{hnf}	kinematic viscosity [m^2/s]
δ_1	velocity slip parameter	$(c_p)_{hnf}$	specific heat [m2/s^{-2}(−|-) K^{-1}]
β_t	thermal slip parameter	α_{hnf}	thermal diffusivity [m^2 s^{-1}]
K_s^*	heterogeneous reaction parameter	ρ_{hnf}	density [kgm^{-3}]
P_m	Porosity parameter	μ_{hnf}	dynamic viscosity [kgm^{-1} s^{-1}]

1. Introduction

Current societal evolution is primarily determined by how and where energy is transported. Energy improvements have a big effect on the fields of industry and engineering. When nanoparticles are added to a regular fluid (like water, glycol, or engine oil), the thermal capacitance of the base fluid goes up. This makes the energy transport mechanism better. Nanofluids are often used in things that help the community, such as nuclear power plants, photovoltaic cells, refrigeration units, thermal exchangers, automobiles, etc. Choi and Eastman first proposed the concept of nanofluid (Choi and Eastman, 1995). Saidur et al. (Saidur et al., 2011) looked into the advanced and new ways nanofluid can be used in home refrigerators, power engines, and chillers. RamReddy et al. (RamReddy et al., 2013) looked at how a semi-infinite vertical plate floating in a nanofluid would handle thermal and solutal energy transmission. Fakour et al. (Fakour et al., 2015) looked at MHD nanofluid flow in a porous canal about heat and transport. Yasir et al. (Yasir et al., 2021) examined the axisymmetric flow of an Oldroyd-B nanofluid caused by a stretched cylinder, accounting for temperature and solute transportation. Using a permeable, contracting surface, Khan et al. (Khan et al., 2021) studied the radiative inflow of light into the nanofluid. In addition, theoreticians in the Refs (Khan and Nadeem, 2021; Khan et al., 2021; Yasir et al., 2022) have experience working in a related field. Improved heat transfer and thermal conductivity in convective fluids are the primary applications for hybrid nanofluids. Convective heat transfer can be enhanced by using hybrid nanofluids, which are generated when various nanoparticles are dissolved in a base fluid. Hybrid nanofluids, as proposed by Turcu et al. (Turcu et al., 2006) and Jana et al. (Jana et al., 2007), increase nanofluids' thermal capacitance. Devi and Devi (Devi and Devi, 2016) presented the improvement of heat transport by scattering water-based Aluminum and copper hybrid nanomaterials subject to stretchable surface. Maskeen et al. (Maskeen et al., 2019) were able to work out the aspects of heat and solutal transfer of hybrid nanofluids composed of alumina, copper, and water that are directed toward the stretched cylinder. Thermal conductivity enhancement of a hybrid nanofluid over a shrinking surface was discussed by Yasir et al. (Yasir et al., 2022). One can find in the references a large study that moves in the direction of a hybrid nanofluid. (Acharya et al., 2019; Qin et al., 2022; Gumus et al., 2016; Waini et al., 2022).(See Table 1.)

Both viscous and non-Newtonian fluids contribute to the fluid flow (having time-dependent or time-independent viscosity). Water and air are just two examples of the many natural fluids considered Newtonian fluids for scientific investigation. After fluid dynamics destabilized the Newtonian framework, there was a strong call for a new theoretical framework. Non-Newtonian fluids have widespread use in various industries and engineering fields, including metalworking, petroleum extraction, the pipe industry, and many others, the literature on non-Newtonian fluid flows across a stretching cylinder is quite substantial. Pseudo-plastic fluids have been the subject of several proposed models for analysis. Different fluid models are offered, including the Cross model (Huang et al., 2022), the Carreau model (Shah et al., 2022), the Power law model (Alhowaity et al., 2022), the Ellis model (Ahmed et al., 2022) the Williamson model (Jalili et al., 2022), and Rabinowitsch fluid (Haider and Ahmad, 2022). There are distinguishing features of each model. The behavior of a viscous fluid flow at a lower shear stress can be predicted by an Ellis fluid, while an Ellis fluid may indicate the behavior of an Ostwald de Waele fluid (Ramzan et al., 2021) at higher shear stresses. The shear thinning and thickening properties of the Ellis fluid is observed at low, intermediate, and high-stress rates. Javed et al. (Javed et al., 2017) looked into the lubrication approximation theory to learn more about Ellis fluid calendaring. Hopke and Slattery (Hopke and Slattery, 1970) determined the upper bounds on drag coefficients for the Ellis fluid attached to a slowly moving sphere. Chhabra et al. (Chhabra et al., 1981) talked about experiments involving a sphere in a crawling motion over an Ellis fluid.

The two main categories of chemical reactions are the heterogeneous and the homogeneous processes. Both homogeneous and heterogeneous responses materialize in many chemical procedures. This is seen in combustion, fog production and dispersion, and catalysis, to name a few. Whereas the homogeneous reaction occurs everywhere in the phase, the heterogeneous reaction happens only in a localized area. Chaudhary and Merkin (Chaudhary and Merkin, 1995) first conceptualized the flow with heterogeneous-homogeneous responses. The MHD Williamson fluid flow around the stagnation point was examined by Ramzan et al. (Ramzan et al., 2017) using a generalized heat flux model, which included both homogeneous and the heterogeneous responses. With a focus on the flow of magnetized Oldroyd-B fluid through a cubic autocatalysis chemical process, Khan et al. (Khan et al., 2022) conducted their research. In addition, researchers have zeroed in on the impact of homo-heterogeneous reactions in their most recent work (see Refs. (Puneeth et al., 2021; Elattar et al., 2022; Gul et al., 2021; Zainal et al., 2021).

Entropy is an essential and measurable statistic often employed by fluid machinists to analyze the irreversible process of processes involving the transfer of mass and heat. The irreversibility of a function is the driving force behind the progression of entropy. (Clausius, 1867) is credited with being the first person to propose the idea of entropy in 1865. It was the result of his substantial examination of the theory of heat and the applications of warmth that he conducted between 1850 and 1864. Carnot's (Carnot, 1978) work catalyzed his creative process. As he began his investigation and worked to build the notion of entropy, that is dictated by the condition of the system.

Table 1 Thermo-physical properties of base-fluid and nano particles (Gumus et al., 2016).

Properties	$\rho\,(kgm^{-3})$	$\sigma\,(\Omega/m)$	$c_p\,(J/Kkg)$	$k\left(W(mk)^{-1}\right)$
$C_2H_6O_2$	1116.6	1.07×10^{-7}	2382	0.249
CuO	6320	5.96×10^{7}	531.5	76.5
Al_2O_3	3970	10^{-10}	765	40

To put it more simply, it measures the unpredictable chaos within a system. Bejan (Bejan, 1979) published research on the formation of entropy in 1979. In his article, he demonstrates that by reducing entropy, the efficiency of a thermal system can be increased. Carrington and Sun initially conceived the term "entropy production" (Carrington and Sun, 1992). According to their theory, entropy is produced whenever there is a significant exchange of heat and mass. Researchers led by Budair (Budair, 2001) looked at fluid friction's effects on entropy when applied to an unstable viscous fluid in the presence of a moving flat plate. According to his studies, the likelihood of entropy effects occurring near the beginning of a movement is higher. The impact of a laminar fluid film being propelled by gravity and passing in front of a heated plate that is angled at an angle was investigated by Sauli and Sauli (Saouli and Aïboud-Saouli, 2004). They proved that addressing the impacts of viscous dissipation led to an improvement in the consequences of entropy propagation. In an elliptic pipe with viscous dissipation implications, Hooman (Hooman, 2005) investigated the generation of entropy in a fully restricted convective surface via porous medium. The flow was observed to be completely contained.

Hybrid nanofluids, which can contain two or more distinct nanoparticle kinds, have recently been introduced for use in thermal transfer. Paraffin oil, gasoline, ethylene glycol, vegetable oil, distilled water, and other solid compounds might be found in these fluids. Hybrid nanofluids have been shown to be helpful in many thermal management applications, including mini/micro transmission thermal sinks, tube and shell exchangers, air conditioning units, tubular heat exchangers, looped heat exchangers, tube in tube, and spiral heat exchangers. Even though this topic hasn't gotten enough concentration, several experimenters have looked at nanofluids in different shapes recently. Akilu et al. (Akilu et al., 2018) studied the flow of silica sulphide and metals oxide hybrid nanofluids and looked at the properties of glycerol and ethyl alcohol to improve the spread of solar energy. Verma et al. (Verma et al., 2018) did an in-depth analysis of how well hybrid nanofluids work in solar collectors as an outstanding working fluid. Rana et al. (Rana and Gupta, 2022) studied the radiative flow of hybrid nanomaterials subject to rotating cone. The research related on the hybrid nanomaterials may be found in the cited works (Rana et al., 2021; Ramesh et al., 2021; Rana et al., 2022; Rana et al., 2022; Bhattacharyya and Gorla, 2013; Rana and Gupta, 2022).

The motivation for this study is to learn more about the 2D boundary layer flow of Ellis nanofluid ($CuO - Al_2O_3$ nanoparticles) over the horizontal, porous, stretched cylinder when the boundary conditions are convective and slip. Viscoelastic dissipation, joule heating, and homo-heterogeneous processes are studied for heat and mass transfer. These results are novel because they examine a previously unexplored aspect of the flow of axisymmetric MHD Ellis hybrid nanofluids. the entropy generation impact along homogeneous-heterogeneous processes. We can transform the initially formulated equations into an ODE system by using similarity variables. By utilizing the in-built method provided by BVP4C in MATLAB, we can numerically address these ODEs. The graphical results can be adjusted following the speed, temperature, and homogeneous/heterogeneous profile. The present results are also good as compared with the previous numerical data.

2. Mathematical modelling

In this mathematical model, we take into account axisymmetric, steady, 2D, laminar, MHD bioconvective Ellis hybrid nanofluid flow with $CuO - Al_2O_3$ nanoparticles over the horizontal porous stretching cylinder. The chemical species that are homogenous and heterogeneous are used to examine the solutal energy transport phenomena. Further, the effects of Joule heating, thermal radiation, and viscous dissipation are taken into account to examine the thermal energy transport features. On the surface of cylinder, the multiple slip boundary conditions are imposed. The cylindrical coordinates system is chosen as $z-$ axis and axis perpendicular to cylindrical surface is taken as $r-$ axis, which is displayed in Fig. 1. The magnetic field applied normal to the surface, which is considered asB_0. The velocity for the fluid is consider as$u = u_w = \frac{zu_0}{L}$, in which $u_0 > 0$ and is L characteristics length. Additionally, the cylindrical surface temperature and microorganism density is T_w and N_w and away from the surface they are T_∞ and N_∞ respectively.

The process of homo-heterogenous reaction equations are defined as,

$$2D + C \to 3D, rate = b^2 a k_c. \tag{1}$$

The 1st order isothermal single response is stated as,

$$C \to D, rate = a k_s. \tag{2}$$

The substance species with concentrations a and b are represents by C and D respectively. Furthermore, the constant rates are k_c and k_s respectively.

The mathematical flow model by using the assumptions discussed above and the boundary layer approximation is followed as,

$$\frac{\partial(ru)}{\partial z} + \frac{\partial(rw)}{\partial r} = 0, \tag{3}$$

$$w\frac{\partial u}{\partial r} + u\frac{\partial u}{\partial z} = \frac{1}{r\rho_{hnf}}\frac{\partial}{\partial r}\left(\frac{r\mu_{hnf}}{1 + \left(\frac{1}{\sqrt{2}\tau_0^2}\frac{\partial u}{\partial r}\right)^{\alpha_1 - 1}}\right) - \left(\frac{\sigma_{hnf}B_0^2}{\rho_{hnf}} + \frac{\mu_{hnf}}{\rho_{hnf}K}\right)u, \tag{4}$$

$$w\frac{\partial T}{\partial r} + u\frac{\partial T}{\partial z} = \alpha_{hnf}\left(\frac{1}{r}\frac{\partial T}{\partial r} + \frac{\partial^2 T}{\partial r^2}\right) + \frac{\mu_{hnf}}{(\rho c_p)_{hnf}}\frac{\partial}{\partial r}\left(\frac{1}{1 + \left(\frac{1}{\sqrt{2}\tau_0^2}\frac{\partial u}{\partial r}\right)^{\alpha_1 - 1}}\right)\left(\frac{\partial u}{\partial r}\right)^2 + \frac{Q_0(T - T_\infty)}{(\rho c_p)_{hnf}} - \frac{1}{(\rho c_p)_{hnf}}\frac{\partial}{\partial r}\left(-\frac{16\sigma^*}{3k^*k}T^3\frac{\partial T}{\partial r}\right) + \frac{\sigma_{hnf}B_0^2}{(\rho c_p)_{hnf}}u^2, \tag{5}$$

$$u\frac{\partial a}{\partial z} + w\frac{\partial a}{\partial r} = D_A^*\left(\frac{1}{r}\frac{\partial a}{\partial r} + \frac{\partial^2 a}{\partial r^2}\right) - k_1 ab^2 - SK_s a, \tag{6}$$

$$+u\frac{\partial b}{\partial z} + w\frac{\partial b}{\partial r} = D_B^*\left(\frac{1}{r}\frac{\partial b}{\partial r} + \frac{\partial^2 b}{\partial r^2}\right) + k_1 ab^2 + SK_s a, \tag{7}$$

$$w\frac{\partial N}{\partial r} + u\frac{\partial N}{\partial z} + \frac{\tilde{b}\,W_c}{\Delta a}\left(\frac{N}{r}\frac{\partial a}{\partial r} + N\frac{\partial^2 a}{\partial r^2} + \frac{\partial N}{\partial r}\frac{\partial a}{\partial r}\right) = D_n\left(\frac{1}{r}\frac{\partial N}{\partial r} + \frac{\partial^2 N}{\partial r^2}\right). \tag{8}$$

The appropriate conditions at the surface of cylinder are,

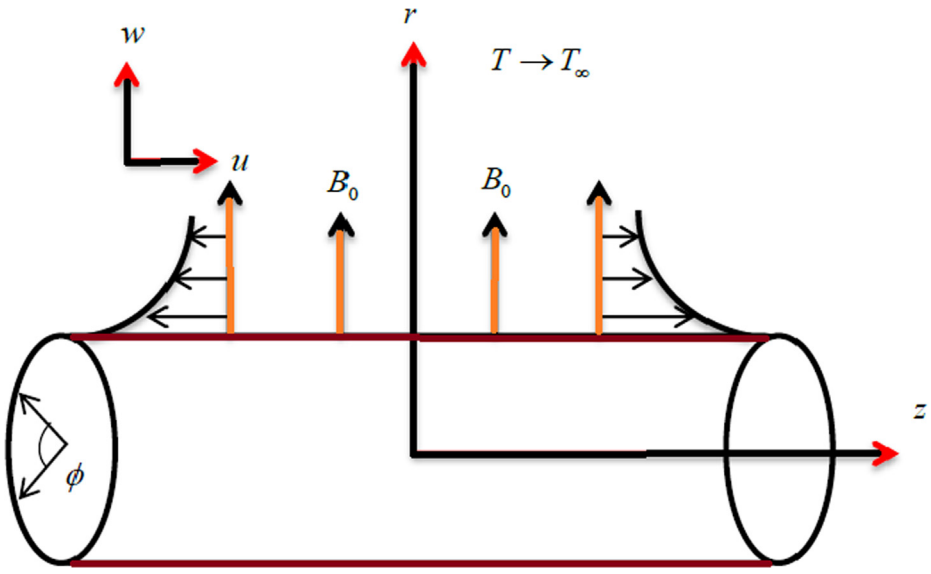

Fig. 1 Diagram of the problem.

$$u = -u_w + a_1\frac{\partial u}{\partial r}, w = -V_w, T = T_w + c_1\frac{\partial T}{\partial r}, \frac{\partial a}{\partial r} = \frac{k_s a}{D_A^*}, \frac{\partial b}{\partial r} = -\frac{k_s a}{D_B^*}, N = N_w + c_2\frac{\partial N}{\partial r}. atr = R. \tag{9}$$

$$u \to 0, a \to a_0, b \to 0, T \to T_\infty, N \to N_\infty, atr \to \infty \tag{10}$$

In the above Eqs. the r, θ, and z having the velocity u, v, and w correspondingly. The involved symbols such asρ_{hnf},μ_{hnf},σ_{hnf},$(\tau_0,\ \alpha_1)$,α_{hnf},c_p,D_n,W_c,$\tilde{b}$,a_1,c_2,k_1, and c_1 are represented the hybrid nanomaterials density, dynamics viscosity, electrical conductivity, material constant, thermal diffusivity, specific heat, microorganism diffusion coefficient, cell swimming speed, chemotaxis constant, factor of velocity slip, microorganism slip factor, constant rate, and temperature slip factor respectively.

2.1. Properties of hybrid nanomaterials

The Himelton Crosser terms for the hybrid nanomaterials are described as.

2.2. Suitable transformations

The similarity variables are stated as,

$$\eta = \frac{r^2-R^2}{2R}\left(\frac{u_w}{zu_f}\right)^{\frac{1}{2}}, u = \frac{zu_0}{L}f'(\eta), w = -\frac{R}{r}\left(\frac{u_0 u_f}{L}\right)^{\frac{1}{2}}f(\eta),$$
$$\psi(\eta, z) = (u_w u_f z)^{\frac{1}{2}}Rf(\eta), \theta(\eta) = \frac{(T-T_\infty)}{(T_w-T_\infty)}, g(\eta) = \frac{a}{a_0}, h(\eta) = \frac{b}{a_0}. \tag{11}$$

Using similarity variables from Eq. (11) and Table 2, the Eqs. (4–10) takes the form.

$$\frac{\mu_{hnf}/\mu_f}{\rho_{hnf}/\rho_f}((1+2\eta\gamma)(\alpha_1(\beta f'')^{\alpha_1-1}+1)f''' + \gamma(3+(\beta f'')^{\alpha_1-1}(1+2\alpha_1))f'') - \frac{\mu_{hnf}/\mu_f}{\rho_{hnf}/\rho_f}(1+(\beta f'')^{\alpha_1-1})^2 P_m f' + (((\beta f'')^{\alpha_1-1}+1)^2(ff''-f'^2) - \frac{\sigma_{hnf}/\sigma_f}{\rho_{hnf}/\rho_f}M((\beta f'')^{\alpha_1-1}+1)^2 f') = 0, \tag{12}$$

$$\frac{\mu_{hnf}/\mu_f}{\rho_{hnf}/\rho_f}((1+2\eta\gamma)(\alpha_1(\beta f'')^{\alpha_1-1}+1)f''' + \gamma(3+(\beta f'')^{\alpha_1-1}(1+2\alpha_1))f'') - \frac{\mu_{hnf}/\mu_f}{\rho_{hnf}/\rho_f}(1+(\beta f'')^{\alpha_1-1})^2 P_m f' + (((\beta f'')^{\alpha_1-1}+1)^2(ff''-f'^2) - \frac{\sigma_{hnf}/\sigma_f}{\rho_{hnf}/\rho_f}M((\beta f'')^{\alpha_1-1}+1)^2 f') = 0, \tag{13}$$

$$\frac{1}{S_c}((1+2\eta\gamma)g'' + 2\gamma g\prime) + fg\prime - K_c g h^2 - K_{vs}g = 0, \tag{14}$$

$$\frac{\delta^*}{S_c}\left((1+2\eta\gamma)h'' + 2\gamma h'\right) + fh' + K_c g h^2 + K_{vs}g = 0, \tag{15}$$

$$((1+2\eta\gamma)\chi'' + 2\gamma\chi') + S_b f\chi' - Pe[(1+2\eta\gamma)g'\chi' + (\Omega+\chi)(\gamma g' + (1+2\eta\gamma)g'')] = 0, \tag{16}$$

The related conditions in dimensionless form,

$$\begin{pmatrix} f(\eta) = S_1, f'(\eta) + 1 = \delta_1 f''(\eta), \theta(\eta) = 1 + \beta_T\theta'(\eta), \\ \chi(\eta) = 1 + \beta_n\chi'(\eta), g(\eta) = \frac{1}{K_s^*}g'(\eta), h'(\eta) = \frac{K_s^*}{\delta^*}g(\eta) \end{pmatrix}, \quad at\ \eta \to 0. \tag{17}$$

$$(f'(\eta) \to 0, g(\eta) \to 1, h(\eta) \to 0, \theta(\eta) \to 0,\ \chi(\eta) \to 0), at\ \eta \to \infty. \tag{18}$$

Assume the particle application of both species' substance have same coefficient of diffusion D_A^* and D_B^* i.e. the ratio$D_A^*/D_B^* = 1$, therefore one can write as,

$$h(\eta) + g(\eta) = 1. \tag{19}$$

The combining above Eqs. (14 and 15) to get,

$$\frac{1}{S_c}\left(g'' + 2\eta\gamma g'' + 2\gamma g'\right) - K_c g(g-1)^2 + fg' - K_{vs}g = 0. \tag{20}$$

The conditions at boundary are,

$$g'(0) = K_s^* g(0),\ \ g(\infty) \to 1. \tag{21}$$

In the overhead equations, the involved physical parameters are expressed as, magnetic field parame-

Table 2 Correlations of hybrid nanofluid (Gumus et al., 2016).

Characteristics	Correlations
Dynamic viscosity	$\mu_{hnf} = \frac{\mu_f}{(1-\phi_1)^{2.5}(1-\phi_2)^{2.5}}$,
Density	$\frac{\rho_{hnf}}{\rho_f} = (1-\phi_2)\left\{(1-\phi_1)+\phi_1\frac{\rho_{s1}}{\rho_f}\right\}+\phi_2\frac{\rho_{s2}}{\rho_f}$,
Thermal conductivity	$\frac{k_{hnf}}{k_{bf}} = \left(\frac{(k_{s2}+2k_{bf})-2(\phi_2 k_{bf}-\phi_2 k_{s2})}{(k_{s2}+2k_{bf})+(\phi_2 k_{bf}-\phi_2 k_{s2})}\right)$, $\frac{k_{bf}}{k_f} = \left(\frac{(k_{s1}+2k_f)-2(\phi_1 k_f-\phi_1 k_{s1})}{(k_{s1}+2k_f)+(\phi_1 k_f-\phi_1 k_{s1})}\right)$,
Heat capacity	$\frac{(\rho c_p)_{hnf}}{(\rho c_p)_f} = (1-\phi_2)\left\{(1-\phi_1)+\frac{(\rho c_p)_{s1}}{(\rho c_p)_f}\phi_1\right\}+\frac{(\rho c_p)_{s2}}{(\rho c_p)_f}\phi_2$,
Electrical conductivity	$\frac{\sigma_{hnf}}{\sigma_f} = \left(\frac{(\phi_1\sigma_{s1}+\phi_2\sigma_{s2})(\phi_{hnf})^{-1}+2(\phi_1\sigma_{s1}+\phi_2\sigma_{s2})+2\sigma_f-2\phi_{hnf}\sigma_f}{(\sigma_{s1}\phi_1+\phi_2\sigma_{s2})(\phi_{hnf})^{-1}+2\sigma_f-(\sigma_{s1}\phi_1+\phi_2\sigma_{s2})+\phi_{hnf}\sigma_f}\right)$.

ter$\{M=\sigma_f B_0^2 z/\rho_f u_w\}$, suction parameter $\left\{S_1=V_w\left(\frac{L}{a\nu_f}\right)^{\frac{1}{2}}>0\right\}$, thermal slip parameter$\left\{\beta_T=c_1\left(\frac{a}{L\nu_f}\right)^{\frac{1}{2}}\right\}$, velocity slip parameter$\left\{\delta_1=a_1\left(\frac{a}{L\nu_f}\right)^{\frac{1}{2}}\right\}$, Porosity parameter$\left\{P_m=\frac{z\mu_f}{Ku_w}\right\}$, Schmidt number$\left\{S_c=\frac{\nu_f}{D_A^*}\right\}$, heterogeneous reaction parameter$\left\{K_s^*=\frac{k_s}{D_A^*}\left(\frac{L\nu_f}{c}\right)^{\frac{1}{2}}\right\}$, Eckert number$\left\{E_c=\frac{u_w^2}{c_p(T_w-T_\infty)}\right\}$, material parameter$\left\{\beta=\sqrt{\frac{u_0^3 r^2 z^2}{2\tau_0^4 R^2 L^3 \mu_f}}\right\}$, curvature parameter$\left\{\gamma=\sqrt{\frac{L\mu_f}{u_0 R^2}}\right\}$, and Prandtl number$\left\{\mathrm{Pr}=\frac{\nu_f}{\alpha_f}\right\}$, bioconvection Schmidt number$\left\{S_b=\frac{\nu_f}{D_n}\right\}$, Peclet number$\left\{Pe=\frac{\tilde{b}W_c}{D_n}\right\}$.

2.3. Physical quantities

The physical quantities of interest like heat transfer rate, microorganism transfer rate, and skin friction coefficient are very vital for engineering point of view. These quantities are mathematically defined as,

$$Cf_x=\frac{\tau_w}{\frac{1}{2}\rho_{hnf}u_0^2}, Nu_x=\frac{xq_w}{k_{hnf}(T_w-T_\infty)}, Nn_x=\frac{xq_n}{D_n(N_w-N_\infty)} \tag{22}$$

The shear stress and heat and motile microorganism fluxes are defined as,

$$\begin{aligned}\tau_w &= \frac{2\mu_{hnf}\frac{\partial u}{\partial r}}{1+(\frac{\tau_{rr}}{\sqrt{2}\tau_0^2})^{\alpha_1-1}}, q_w \\ &= -k_{hnf}(\frac{\partial T}{\partial r})\Big|_{r=0} - \frac{16\sigma^*}{3k^*}T^3(\frac{\partial T}{\partial r})\Big|_{r=0}, q_n \\ &= -D_n(\frac{\partial N}{\partial r})\Big|_{r=0}.\end{aligned} \tag{23}$$

The dimensionless form of skin friction, Nusselt number, and microorganism number is defined as,

$$Cf_x(Re_x)^{1/2}=\left(2f''(0)-\frac{\sqrt{2}}{\beta}\right)\Big|_{\alpha_1=0},$$

$$Nu_x(\mathrm{Re}_x)^{-1/2}=-(1+R_d)\theta'(0), Nn_x(\mathrm{Re}_x)^{-1/2}=-\chi'(0) \tag{24}$$

Here, Re_x is the Reynold number.

2.4. Entropy generation

The entropy generation equation is written as:

$$\begin{aligned}S_{gen}=\frac{k_{hnf}}{T_\infty^2}\left(1+\frac{16\sigma^* T^3}{3k^* k}\right)\left(\frac{\partial T}{\partial r}\right)^2+\left(\begin{array}{c}\frac{\sigma_{hnf}}{\rho_{hnf}}\frac{B_0^2u^2}{T_\infty}+\frac{RD_A^*}{T_\infty}\left(\frac{\partial T}{\partial r}\right)\frac{\partial a}{\partial r}+\frac{RD_A^*}{a_0}\left(\frac{\partial a}{\partial r}\right)^2\\+\frac{\mu_{hnf}}{kT_\infty}u^2+\frac{RD_B^*}{T_\infty}\left(\frac{\partial b}{\partial r}\frac{\partial T}{\partial r}\right)+\frac{RD_B^* b}{a_0}\left(\frac{\partial b}{\partial r}\right)^2\end{array}\right)\\+\frac{\mu_{hnf}}{T_\infty}\left(\frac{\left(\frac{\partial u}{\partial r}\right)^2}{1+\left(\frac{1}{\sqrt{2}\tau_0^2}\frac{\partial u}{\partial r}\right)^{\alpha_1-1}}\right)+\left(\frac{D_N}{T_\infty}\left(\frac{\partial T}{\partial r}\right)\frac{\partial N}{\partial r}+\frac{D_N}{N_\infty}\left(\frac{\partial N}{\partial r}\right)^2\right)\end{aligned} \tag{25}$$

$$N_G=\frac{S_{gen}}{S_0} \tag{26}$$

The entropy generation N_G is the ratio between S_0(characteristic entropy generation rate) to S_{gen}(entropy generation rate) such that,

$$\begin{aligned}N_G &= \tfrac{k_{hnf}}{k_f}(1+R_d(\theta(T_r-1)+1)^3)(1+2\gamma\eta)\alpha_2\theta'^2+\tfrac{\sigma_{hnf}/\sigma_f}{\rho_{hnf}/\rho_f}MBrf'^2 \\ &+\tfrac{\mu_{hnf}}{\mu_f}\left(\tfrac{Br(1+2\gamma\eta)}{1+(\beta f'')^{\alpha_1-1}}\right)+\left((1+2\gamma\eta)\left(\tfrac{L_1+L_2}{\alpha_2}\right)g'^2+(L_1-L_2)(1+2\gamma\eta)\theta' g'\right) \\ &+(1+2\gamma\eta)\left(\tfrac{L_1+L_2}{\alpha_3}\right)\chi'^2+(L_1-L_2)(1+2\gamma\eta)\theta'\chi'\end{aligned} \tag{27}$$

Where $\alpha_2=\frac{\Delta T}{T_\infty}$ is temperature ratio parameter and $Br=\frac{\mu_f u_w}{k_f\Delta T}$ is Brinkman number. Moreover, L_1 and L_2 is defined as $L_1=\frac{RD_A^* a_0}{k_f}$ and,$L_2=\frac{RD_B^* a_0}{k_f}$.

3. Discussion of graphical results

The numerical explanation of the current problem is procured using the bvp4c MATLAB built-in approach by the consideration of residual error of up to 10^{-6}. In the following section, the influence of different physical flow parameters such as magnetic parameter, curvature parameter, thermal slip parameter, porosity parameter, suction parameter, surface catalyzed parameter, temperature ratio parameter, homogeneous reaction parameter, and Brinkman number on fluid velocity, ther-

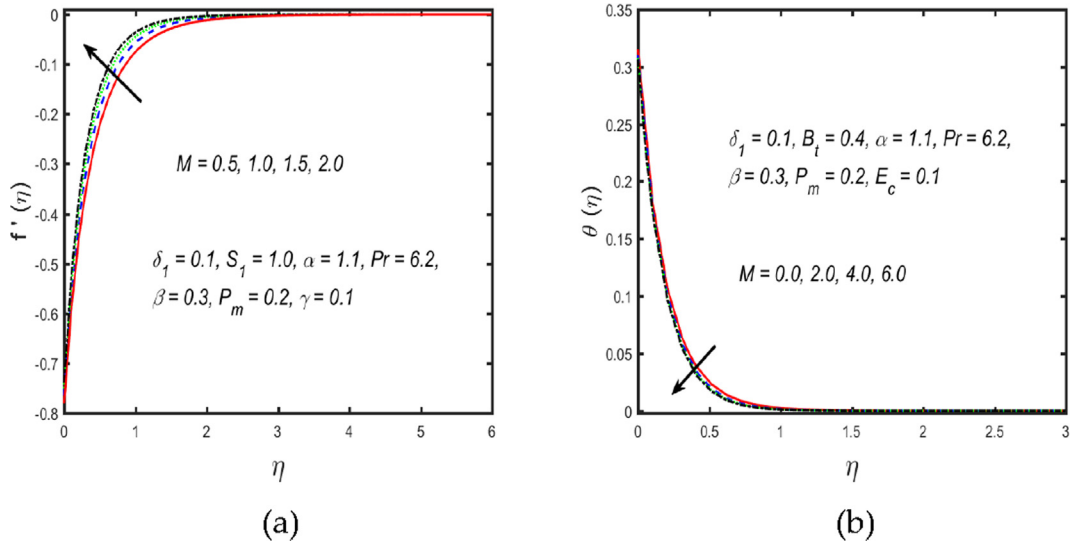

Fig. 2 **(a and b).** Upshots of $f'(\eta)$ and $\theta(\eta)$ for$M$.

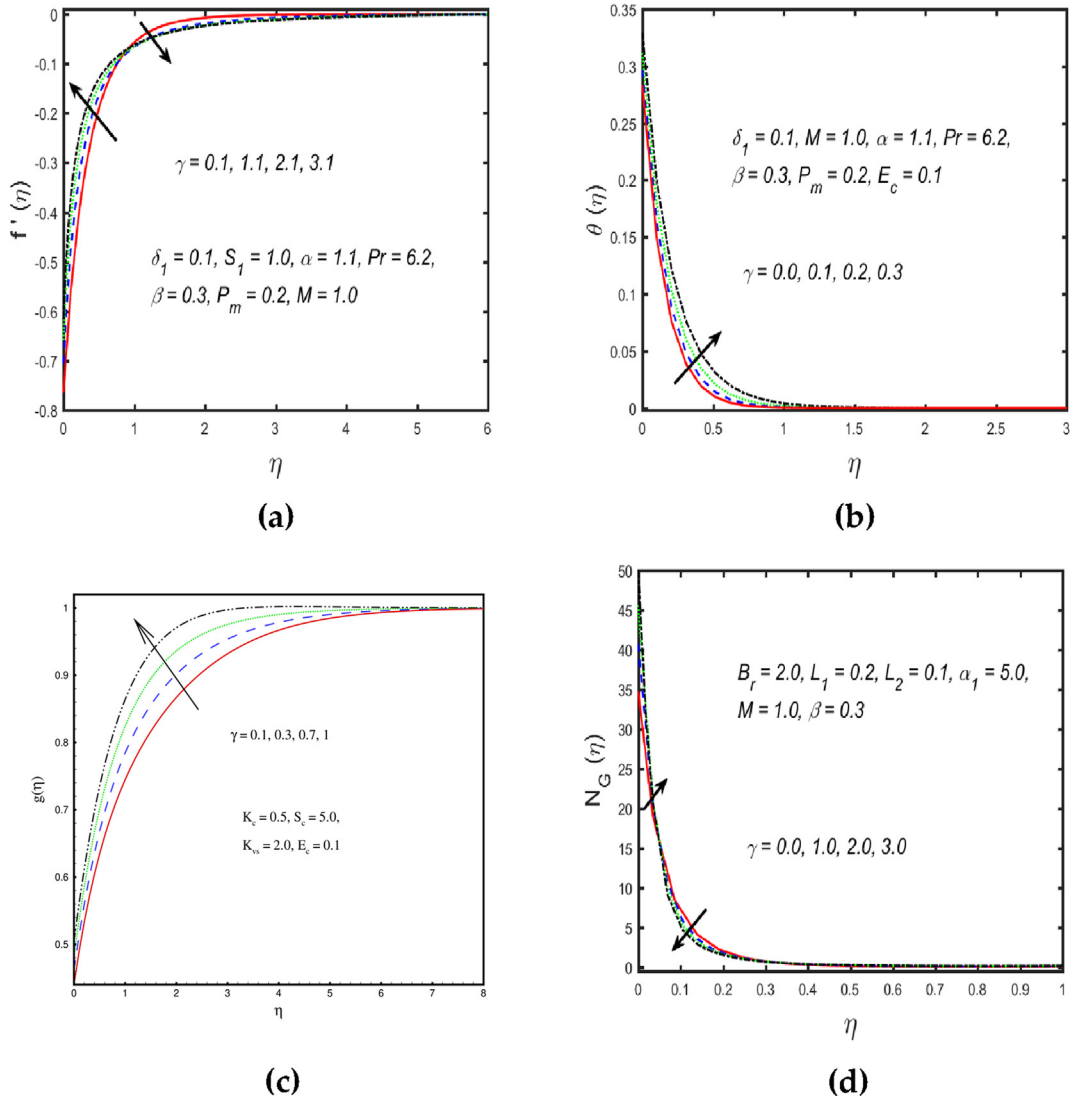

Fig. 3 **(a – d):** Upshots of$f'(\eta)$,$\theta(\eta)$, $g(\eta)$ and $N_G(\eta)$ forγ.

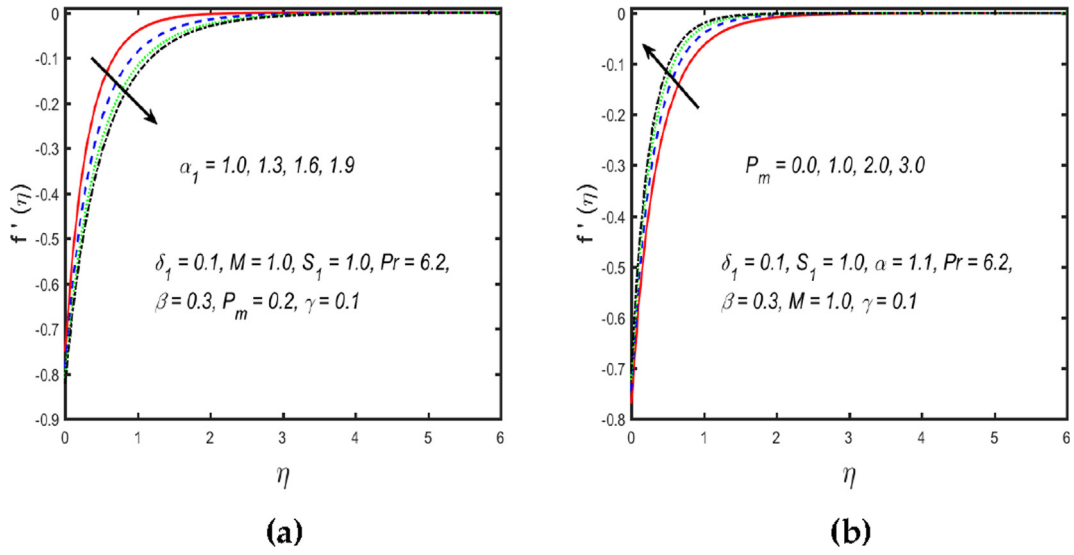

Fig. 4 (a and b). Upshots of $f'(\eta)$ for α_1 and P_m respectively.

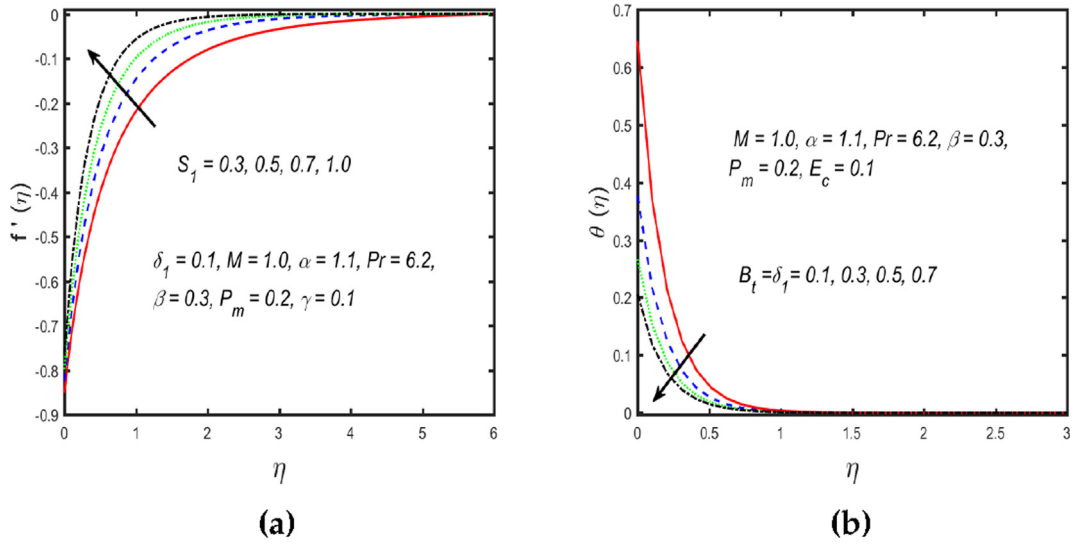

Fig. 5 (a and b). Upshots of $f'(\eta)$ and $\theta(\eta)$ for S_1 and B_t respectively.

mal distribution, concentration reaction, and entropy generation are communicated in Figs. (2 – 7).

The upshot of magnetic parameters on fluid velocity and temperature is discussed in Fig. 2 ((a) and (b)). It is observed that the fluid velocity enhances while their related boundary layer thickness diminishes. This is due to the fact that through increasing the magnetic parameter Lorentz strength occurs, which improves the resistance in motion of the fluid. Therefore, the velocity of hybrid nanomaterials shows decreasing behavior. It is clear from Fig. 2 (b) that the temperature of the fluid thickens due to the stronger assessment of the magnetic parameter. The effects of the curvature parameter on fluid velocity, thermal, homogeneous/heterogeneous reaction, and entropy generation profile are shown in Fig. 3 (a–d). From Fig. 3(a), it is seen that the velocity field portrays a dual trend by the increment of the curvature parameter. The fluid velocity boosts around the surface as the curvature parameter's value rises, while it drops away from the boundary. Physically, the cylinders have an inverse relationship between their radius and curvature. As a result, as the curvature parameter increases, the cylinder's radius decreases. Thus, the connection of Ellis liquid along the surface of the cylinder diminished. Consequently, the surface sustains a minor level of resistance due to fluid particles. As a result, a large increment in the curvature parameter γ asymptotically declines in the velocity of fluid. Fig. 3 (b) depicts how fluid temperature grows as the γ is increased. The augmenting values of γ (curvature parameter), physically reflect a rise in the thermal boundary layer thickness, implying that heat transportations and therefore boosts temperature distribution. Likewise, increasing the γ enhances the graphical behavior of concentration and entropy generation distributions, which is displayed in Fig. 3 ((c) and

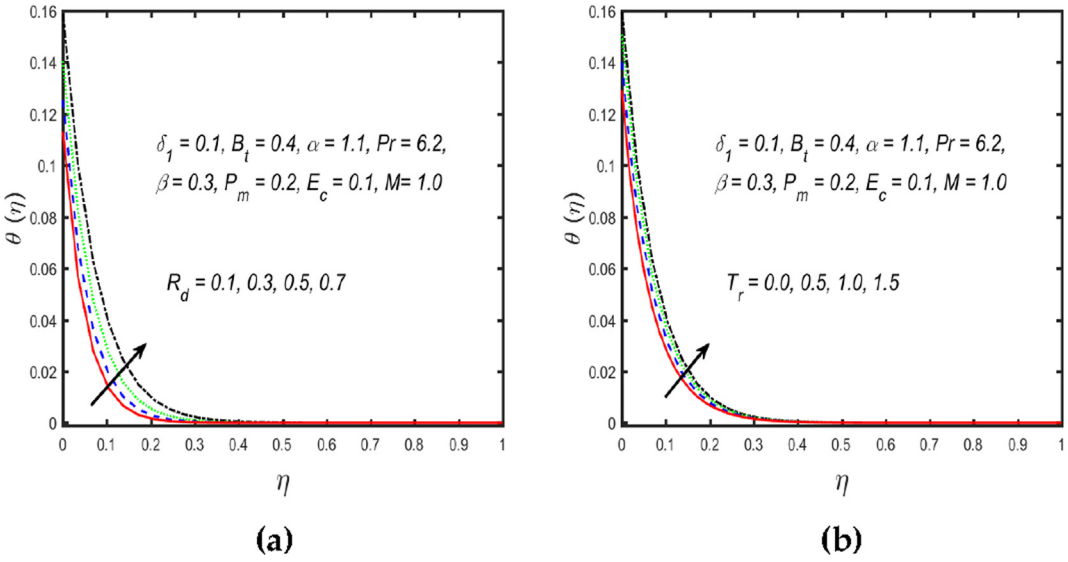

Fig. 6 (a and b). Upshots of $\theta(\eta)$ for R_d and T_r respectively.

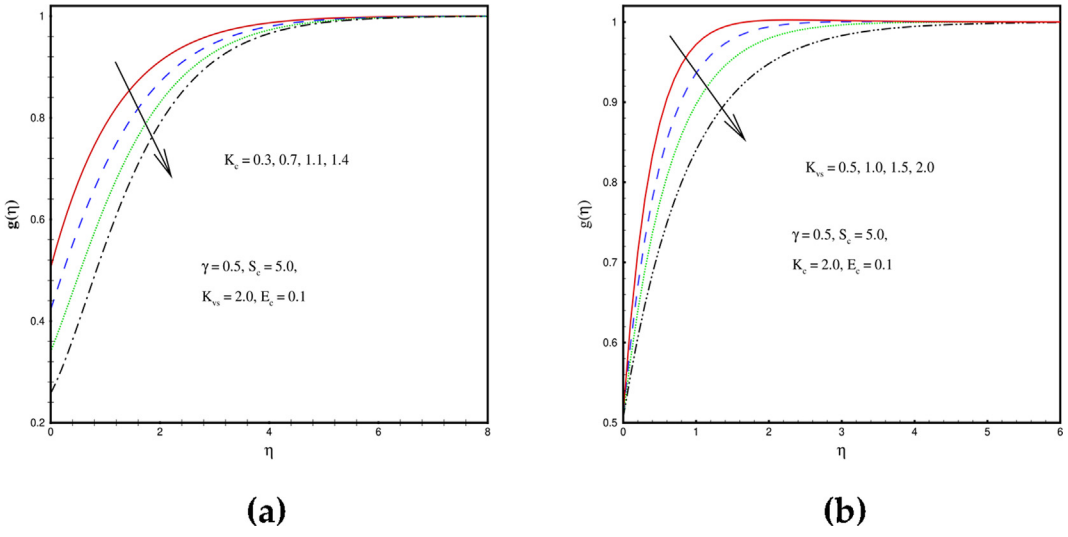

Fig. 7 **(a and b).** Upshots of $g(\eta)$ for K_c and K_{vs} respectively.

(d)). Fig. 4 ((a) and (b)) depict the upshots of material and porosity parameters on the velocity profile. The consequence of the material invariant is kept in Fig. 4(a). The velocity reduces and their related boundary layer thickness upsurges with the improved value of the material parameter. Fig. 4(b) depicts the impact of P_m on the velocity profile of the Ellis hybrid nanomaterials. The momentum boundary layer shrinks as the liquid phase's porosity increases, which is consistent with reality. The consequences of the S_1 (suction parameter) and B_t (thermal slip parameter) on velocity and temperature distribution are discussed in Fig. 5 ((a) and (b) correspondingly. Fig. 5 (a) looks at velocity characteristics in order to get a more reasonable estimation of a suction parameter. This seems to be resulting in a reduction in the thickness of the momentum boundary layer. Physically, When the suction parameter is raised, the drag force emerges, which reduces the thickness of the related boundary layers. According to Fig. 5 ((a) and (b)), the wall temperature declines as the velocity and thermal slips rises. The increasing thermal slip parameter causes a decaying phenomenon in the surface area of the temperature layer, which demonstrating that small amount of heat is transmitted to the fluids that has released from the wall. While the velocity slip partially reflected the increase in dragging strength on the stretching wall as it moved toward the liquid. Fig. 6((a) and (b)) closely examined the effects of solar radiation and temperature ratio parameter on thermal distribution. Fig. 6(a) demonstrates how the temperature field and thermal boundary layer that are related to it are enhanced when the radiation parameter is given a higher value. The fluid temperature rises if the radiation parameter is high because the fluid is being physically heated more and more. Fig. 6 depicts the temperature variation for the particular values of temperature ratio parameter value (b). In this situation, a rise in the temperature ratio parameter leads to an increase in the temperature gradient. The strength of the homogeneous reaction parameter as shown on the $g(\eta)$ sketch is depicted in Fig. 7

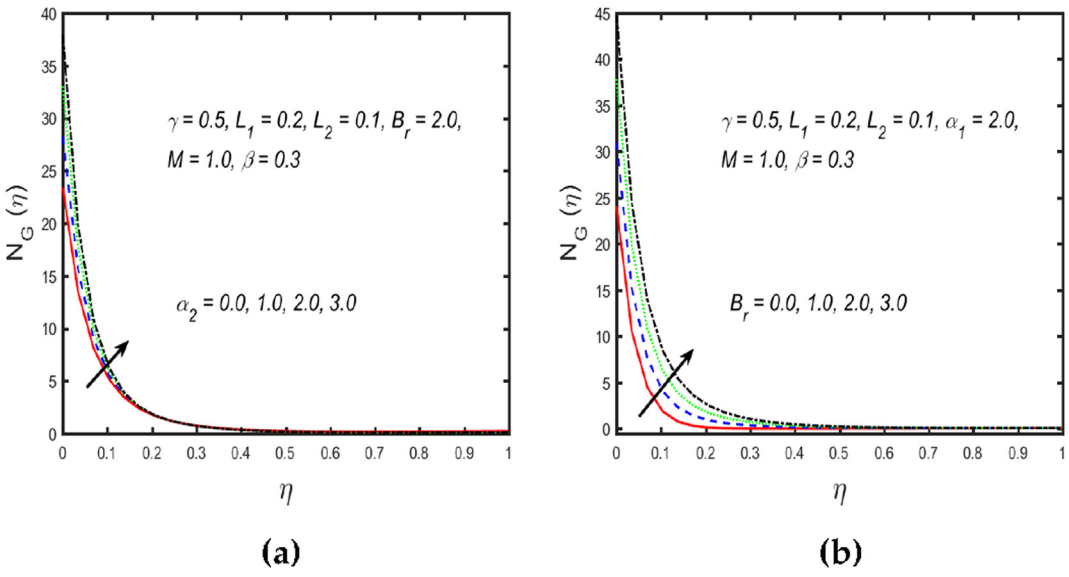

Fig. 8 **(a and b).** Upshots of $N_G(\eta)$ for α_2 and Br respectively.

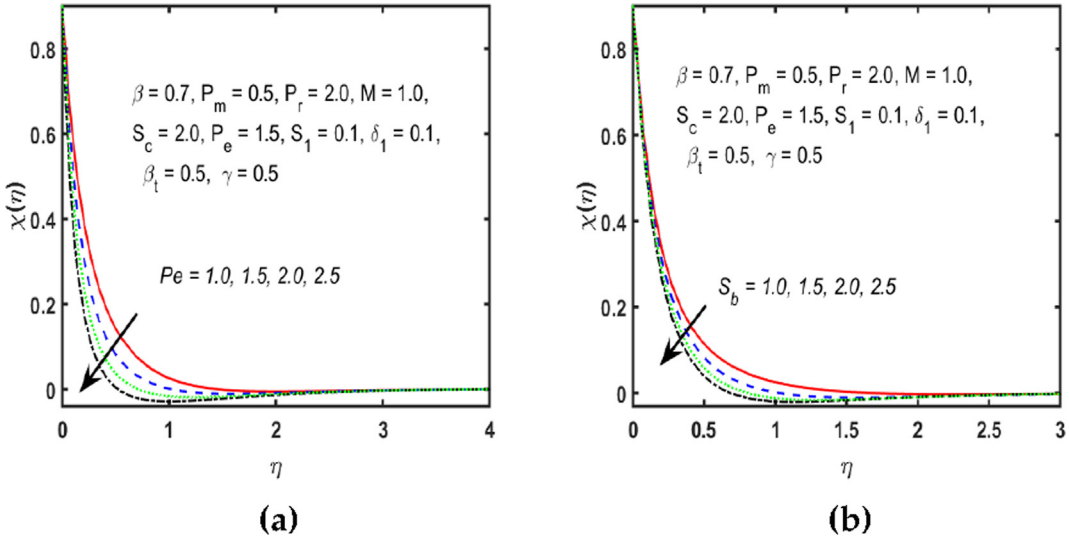

Fig. 9 (a and b). Upshots of $\chi(\eta)$ for Pe and S_b respectively.

(a). With an increase in homogeneous reaction parameters, the behavior of $g(\eta)$ degrades. Fig. 7(b) shows how the sketch $g(\eta)$ for the surface catalyzed reaction performed. By using porous media, the reactants gain more surface region for the response to proceed. The surface-catalyzed reaction accelerates the reaction rate further. As a result, a faster decrease in the $g(\eta)$ sketch occurs when the surface catalyzed reaction is increased. The effects of the temperature ratio parameter and the Brinkman number on entropy generation are investigated in Fig. 8 ((a) and (b)). These figures show that increasing the Brinkman number, and ratio parameter boosts the entropy in the system. The fluid's velocity is opposed by the Lewis number due to bioconvection, which causes a sharp drop in profile as seen in Fig. 9(a). Higher S_b values lower microorganism diffusivity, which lowers the motile density because, mathematically speaking, bioconvective have an inverse relationship with microorganism diffusivity. Fig. 9(b) incorporates the Peclet number Pe characteristics through rescaled microorganism distribution. It demonstrates how, as the bioconvection Peclet number Pe rises, the microorganism profile decreases. Pe is the mathematical expression for the relationship between the thermal energy that is transferred into the fluid and the thermal energy that is convicted to the fluid. The constant chemotaxis correlates oppositely with microorganism diffusivity, and as a result, Pe contains relationships through maximum cell swimming movement. Therefore, the microorganism's profile will be wider for higher values ofPe. A comparison is performed between the present numerical results and results that are already published Ramesh et al. (Elattar et al., 2022) and Bhattacharya (Gul et al., 2021), which are presented in Tables 3 to confirm that the findings are accurate. This table illustrates a satisfactory similarity among recent simulation solu-

Table 3 The numerical values $f''(0)$ in non-existence of$\alpha_1,\beta,\phi_1,\phi_2$ and$S_1 = 2.6, \Pr = 0.5$.

γ	Ramesh et al. (Ramesh et al., 2021)	Battacharya (Bhattacharyya and Gorla, 2013)	Present result
0.1	2.100332	2.1003187	2.10034
0.2	2.058843	2.0588875	2.05886
0.3	2.008887	2.0088406	2.00885

Table 4 The variation in skin friction against the various parameters.

γ	M	β	P_m	$Cf_x(Re_x)^{\frac{1}{2}}$
0.1				−1.1915497
0.3				−0.7484242
0.5				−0.5976694
	0.0			−0.4246229
	1.0			−0.5152779
	2.0			−0.5898416
		0.0		−1.4895497
		1.0		−0.6981293
		2.0		−0.5411256
			1.0	−0.4979585
			2.0	−0.5838998
			3.0	−0.6492439

Table 5 Variation in Nusselt number against the various parameters.

γ	M	R_d	E_c	$Nu_x(Re_x)^{-\frac{1}{2}}$
0.1				−0.1145219
0.3				−0.1165937
0.5				−0.1173313
	0.0			−0.1156889
	1.0			−0.1173368
	2.0			−0.1182346
		0.0		−0.1239312
		1.0		−0.1199315
		2.0		−0.1159669
			1.0	−0.1224298
			2.0	−0.1129244
			3.0	−0.1117746

tion and earlier outcomes. This guarantees the accuracy of our numerical reports. Further, the calculated numerical values for skin friction coefficient and local Nusselt number are presented in Table 4 and Table 5 against the various parameters. It seen from the tables, that by the greater values of M **and** P_m**, the increment is occurs in the skin friction coefficient, but reverse trend is noted for** γ **and**β **. Further, heat transfer rate improves for the higher values of** M **and**R_d**.**

4. Concluding remarks

The flow of hybrid nanomaterials $CuO - Al_2O_3/C_2H_6O_2$ in a permeable porous cylinder is explored by combining homogeneous/heterogeneous processes with Ohmic heating, and the slip conditions. The nonlinear differential equations are solved numerically with the help of the bvp4c technique in MATLAB. The pursuing are the elucidations of this analysis:

- The curvature parameter exhibits a dual behavior with respect to fluid velocity and entropy production.
- With stronger porosity and magnetic parameter estimation, the thickness of the momentum boundary layer decreases.
- The fluid velocity increases as the suction parameter are increased, while it decreases as the material parameter is increased.
- The surface-catalyzed and homogeneous reaction parameters have improved, resulting in a low fluid concentration.
- The increased values of the temperature ratio parameter and radiation parameter increased the fluid temperature.
- The temperature distribution is reduced by thermal and velocity slip parameters.
- The microorganism profile declined with the increment of Peclet number and bioconvection Schmidt number.
- The heat transfer rate and shear rate declined with the improvement of magnetic field parameter.

Declaration of Competing Interest

The authors declare that they have no known competing financial interests or personal relationships that could have appeared to influence the work reported in this paper.

Acknowledgments

The authors extend their appreciation to the Deanship of Scientific Research at King Khalid University for funding this work through the Research Groups Program under grant number RGP.2/57/43.

References

Acharya, N., Maity, S., Kundu, P.K., 2019. Framing the hydrothermal features of magnetized TiO2–CoFe2O4 water-based steady hybrid nanofluid flow over a radiative revolving disk. Multidiscip. Model. Mater. Struct. 16 (4).

Ahmed, S.E., Arafa, A.A., Hussein, S.A., 2022. MHD Ellis nanofluids flow around rotating cone in the presence of motile oxytactic microorganisms. Int. Commun. Heat Mass Transfer 134, 106056.

Akilu, S., Baheta, A.T., Said, M.A.M., Minea, A.A., Sharma, K.V., 2018. Properties of glycerol and ethylene glycol mixture based SiO2-CuO/C hybrid nanofluid for enhanced solar energy transport. Sol. Energy Mater. Sol. Cells 179, 118–128.

Alhowaity, A., Bilal, M., Hamam, H., Alqarni, M.M., Mukdasai, K., Ali, A., 2022. Non-Fourier energy transmission in power-law hybrid nanofluid flow over a moving sheet. Sci. Rep. 12 (1), 1–12.

Bejan, A. (1979). A study of entropy generation in fundamental convective heat transfer.

Bhattacharyya, K., Gorla, R.S.R., 2013. Boundary layer flow and heat transfer over a permeable shrinking cylinder with surface mass transfer. Int. J. Appl. Mech. Eng. 18 (4).

Budair, M.O., 2001. Entropy analysis of unsteady flow on flat plate. Int. J. Energy Res. 25 (6), 519–524.

Carnot, S. (1978). *Reflections on the Motive Power of Fire* (No. 26). Vrin

Carrington, C.G., Sun, Z.F., 1992. Second law analysis of combined heat and mass transfer in internal and external flows. Int. J. Heat Fluid Flow 13 (1), 65–70.

Chaudhary, M.A., Merkin, J.H., 1995. A simple isothermal model for homogeneous-heterogeneous reactions in boundary-layer flow. I equal diffusivities. *Fluid Dyn. Res.* 16 (6), 311.

Chhabra, R.P., Tiu, C., Uhlherr, P.H.T., 1981. Creeping motion of spheres through Ellis model fluids. Rheol. Acta 20 (4), 346–351.

Choi, S.U. and Eastman, J.A., 1995. *Enhancing thermal conductivity of fluids with nanoparticles* (No. ANL/MSD/CP-84938; CONF-951135-29). Argonne National Lab., IL (United States).

Clausius, R. (1867). Uber verschiedene für die Abwendung bequeme Formen der Haupt-gleichungen der mechanischen Wärmetheorie. Vierteiljahrschrift der Naturforschenden Gesselschaft (Zürich) 1865 [Chapter X (on several convenient forms of the fundamental equations of the mechanical theory of heat)]. *The mechanical theory of heat. with its applications to the steam engine and to physical properties of bodies. London. John van Voorst*, 1-59.

Devi, S.A., Devi, S.S.U., 2016. Numerical investigation of hydromagnetic hybrid Cu–Al2O3/water nanofluid flow over a permeable stretching sheet with suction. Int. J. Nonlinear Sci. Numer. Simul. 17 (5), 249–257.

Elattar, S., Helmi, M.M., Elkotb, M.A., El-Shorbagy, M.A., Abdelrahman, A., Bilal, M., Ali, A., 2022. Computational assessment of hybrid nanofluid flow with the influence of hall current and chemical reaction over a slender stretching surface. Alexand. Eng. J. 61 (12), 10319–10331.

Fakour, M., Ganji, D.D., Abbasi, M., 2015. Investigation of nanofluid MHD flow and heat transfer in a channel. J. Adv. Phys. 4 (1), 46–56.

Gul, H., Ramzan, M., Chung, J.D., Chu, Y.M., Kadry, S., 2021. Multiple slips impact in the MHD hybrid nanofluid flow with Cattaneo-Christov heat flux and autocatalytic chemical reaction. Sci. Rep. 11 (1), 1–14.

Gumus, S., Ozcan, H., Ozbey, M., Topaloglu, B., 2016. Aluminum oxide and copper oxide nanodiesel fuel properties and usage in a compression ignition engine. Fuel 163, 80–87.

Haider, J.A., Ahmad, S., 2022. Dynamics of the Rabinowitsch fluid in a reduced form of elliptic duct using finite volume method. Int. J. Mod Phys B, 2250217.

Hooman, K., 2005. Fully developed temperature distribution in a porous saturated duct of elliptical cross section with viscous dissipation effects and entropy generation analysis. Heat Transf. Res. 36 (3).

Hopke, S.W., Slattery, J.C., 1970. Upper and lower bounds on the drag coefficient of a sphere in an Ellis model fluid. AIChE J. 16 (2), 224–229.

Huang, H., Wang, Y., Chen, Z., Zhang, Y., Li, Y., Tang, Z., ... & Ma, K. K. (2022, June). Cmua-watermark. A cross-model universal adversarial watermark for combating deepfakes. In *Proceedings of the AAAI Conference on Artificial Intelligence* (Vol. 36, No. 1, pp. 989-997).

Jalili, B., Ganji, A.D., Jalili, P., Nourazar, S.S., Ganji, D.D., 2022. Thermal analysis of Williamson fluid flow with Lorentz force on the stretching plate. Case Stud. Therm. Eng., 102374

Jana, S., Salehi-Khojin, A., Zhong, W.H., 2007. Enhancement of fluid thermal conductivity by the addition of single and hybrid nano-additives. Thermochim. Acta 462 (1–2), 45–55.

Javed, M.A., Ali, N., Sajid, M., 2017. A theoretical analysis of the calendering of Ellis fluid. J. Plast. Film Sheeting 33 (2), 207–226.

Khan, M., Ahmad, L., Yasir, M., Ahmed, J., 2021. Numerical analysis in thermally radiative stagnation point flow of Cross nanofluid due to shrinking surface. dual solutions. Appl. Nanosci., 1–12

Khan, M.N., Nadeem, S., 2021. A comparative study between linear and exponential stretching sheet with double stratification of a rotating Maxwell nanofluid flow. Surf. Interfaces 22, 100886.

Khan, M.N., Ahmad, S., Nadeem, S., 2021. Flow and heat transfer investigation of bio–convective hybrid nanofluid with triple stratification effects. Phys. Scr. 96, (6) 065210.

Khan, M., Yasir, M., Alshomrani, A.S., Sivasankaran, S., Aladwani, Y.R., Ahmed, A., 2022. Variable heat source in stagnation-point unsteady flow of magnetized Oldroyd-B fluid with cubic autocatalysis chemical reaction. Ain Shams Eng. J. 13, (3) 101610.

Maskeen, M.M., Zeeshan, A., Mehmood, O.U., Hassan, M., 2019. Heat transfer enhancement in hydromagnetic alumina–copper/water hybrid nanofluid flow over a stretching cylinder. J. Therm. Anal. Calorim. 138 (2), 1127–1136.

Puneeth, V., Manjunatha, S., Makinde, O.D., Gireesha, B.J., 2021. Bioconvection of a radiating hybrid nanofluid past a thin needle in the presence of heterogeneous–homogeneous chemical reaction. J. Heat Transf. 143 (4).

Qin, L., Ahmad, S., Khan, M.N., Ahammad, N.A., Gamaoun, F., Galal, A.M., 2022. Thermal and solutal transport analysis of Blasius–Rayleigh–Stokes flow of hybrid nanofluid with convective boundary conditions. Waves Random Complex Medium, 1–19.

Ramesh, G.K., Manjunatha, S., Roopa, G.S., Chamkha, A.J., 2021. Hybrid (ND-Co3O4/EG) nanoliquid through a permeable cylinder under homogeneous-heterogeneous reactions and slip effects. J. Therm. Anal. Calorim. 146 (3), 1347–1357.

RamReddy, C., Murthy, P.V.S.N., Chamkha, A.J., Rashad, A.M., 2013. Soret effect on mixed convection flow in a nanofluid under convective boundary condition. Int. J. Heat Mass Transf. 64, 384–392.

Ramzan, M., Bilal, M., Chung, J.D., 2017. MHD stagnation point Cattaneo-Christov heat flux in Williamson fluid flow with homogeneous–heterogeneous reactions and convective boundary condition—a numerical approach. J. Mol. Liq. 225, 856–862.

Ramzan, M., Riasat, S., Kadry, S., Chu, Y.M., Ghazwani, H.A.S., Alzahrani, A.K., 2021. Influence of autocatalytic chemical reaction with heterogeneous catalysis in the flow of Ostwald-de-Waele nanofluid past a rotating disk with variable thickness in porous media. Int. Commun. Heat Mass Transf. 128, 105653.

Rana, P., Gupta, S., Pop, I., Gupta, G., 2022. Three-dimensional heat transfer of 29 nm CuO-H2O nanoliquid with Joule heating and slip effects over a wedge surface. Int. Commun. Heat Mass Transf. 134, 106001.

Rana, P., Gupta, G., 2022. FEM Solution to quadratic convective and radiative flow of Ag-MgO/H2O hybrid nanofluid over a rotating cone with Hall current. Optimization Using Response Surface Methodology. *Mathematics and Computers in Simulation*.

Rana, P., Gupta, G., 2022. Heat transfer optimization of Marangoni convective flow of nanofluid over an infinite disk with Stefan blowing and slip effects using Taguchi method. Int. Commun. Heat Mass Transf. 130, 105822.

Rana, P., Makkar, V., Gupta, G., 2021. Finite element study of bioconvective Stefan blowing Ag-MgO/water hybrid nanofluid induced by stretching cylinder utilizing non-Fourier and non-Fick's laws. Nanomaterials 11 (7), 1735.

Rana, P., Mahanthesh, B., Thriveni, K., Muhammad, T., 2022. Significance of aggregation of nanoparticles, activation energy, and Hall current to enhance the heat transfer phenomena in a nanofluid. In: a sensitivity analysis. Waves in Random and Complex Media, pp. 1–23.

Saidur, R., Leong, K.Y., Mohammed, H.A., 2011. A review on applications and challenges of nanofluids. Renew. Sustain. Energy Rev. 15 (3), 1646–1668.

Saouli, S., Aïboud-Saouli, S., 2004. Second law analysis of laminar falling liquid film along an inclined heated plate. Int. Commun. Heat Mass Transf. 31 (6), 879–886.

Shah, S.Z.H., Fathurrochman, I., Ayub, A., Altamirano, G.C., Rizwan, A., Núñez, R.A.S., Yeskindirova, M., 2022. Inclined magnetized and energy transportation aspect of infinite shear rate viscosity model of Carreau nanofluid with multiple features over wedge geometry. Heat Transf. 51 (2), 1622–1648.

Turcu, R., Darabont, A.L., Nan, A., Aldea, N., Macovei, D., Bica, D., Vekas, L., Pana, O., Soran, M.L., Koos, A.A., Biro, L.P., 2006. New polypyrrole-multiwall carbon nanotubes hybrid materials. J. Optoelectron. Adv. Mater. 8 (2), 643–647.

Verma, S.K., Tiwari, A.K., Tiwari, S., Chauhan, D.S., 2018. Performance analysis of hybrid nanofluids in flat plate solar collector as an advanced working fluid. Sol. Energy 167, 231–241.

Waini, I., Khan, U., Zaib, A., Ishak, A., Pop, I., 2022. Thermophoresis particle deposition of CoFe2O4-TiO2 hybrid nanoparticles on micropolar flow through a moving flat plate with viscous dissipation effects. Int. J. Numer. Meth. Heat Fluid Flow.

Yasir, M., Ahmed, A., Khan, M., Ullah, M.Z., 2021. Convective transport of thermal and solutal energy in unsteady MHD Oldroyd-B nanofluid flow. Phys. Scr. 96, (12) 125266.

Yasir, M., Hafeez, A., Khan, M., 2022. Thermal conductivity performance in hybrid (SWCNTs-CuO/Ehylene glycol) nanofluid flow. dual solutions. *Ain Shams Eng. J.* 13, (5) 101703.

Yasir, M., Ahmed, A., Khan, M., Alzahrani, A.K., Malik, Z.U., Alshehri, A.M., 2022. Mathematical modelling of unsteady Oldroyd-B fluid flow due to stretchable cylindrical surface with energy transport. Ain Shams Eng. J. 101825

Zainal, N.A., Nazar, R., Naganthran, K., Pop, I., 2021. Flow and heat transfer over a permeable moving wedge in a hybrid nanofluid with activation energy and binary chemical reaction. Int. J. Numer. Meth. Heat Fluid Flow.